Geophysical Journal International

Geophys. J. Int. (2022) **229,** 1462–1473
Advance Access publication 2022 January 8
GJI Seismology

https://doi.org/10.1093/gji/ggac006

Anisotropic elastic parameter estimation from multicomponent ground-motion observations: a theoretical study

S. Noe [1,*] S. Yuan [1] J.-P. Montagner[2] and H. Igel[1]

[1]*Department of Earth and Environmental Sciences, Ludwig-Maximilian University, Munich, 80333 München, Germany. E-mail: sebastian.noe@erdw.ethz.ch*
[2]*Institut de Physique du Globe de Paris, Université de Paris, 7154, Paris, France*

Accepted 2022 January 5. Received 2021 October 19; in original form 2021 June 11

SUMMARY

We investigate the potential of multicomponent, single-point ground-motion observations (displacement, rotation and strain) to allow the estimation of near-receiver anisotropic elastic parameters. Based on full-space, plane-wave propagation analysis, we demonstrate that in (locally homogeneous) anisotropic media, the wave propagation direction and the velocities of quasi-*P* and quasi-*S* waves can—in principle—be determined from three components of displacements and three components of rotations. Mimicking the situation of a borehole setting, we formulate an inverse problem, estimating the full elastic tensor from multidirectional observations. We show that in the presence of noise it is beneficial to observe additionally a longitudinal strain component (e.g. along the borehole), further constraining the predominantly quasi-*P* related elastic tensor components.

Key words: Joint inversion; Rotational seismology; Seismic anisotropy; Theoretical seismology.

1 INTRODUCTION

Even though seismic anisotropy—the directional dependence of propagation velocities in a homogeneous elastic medium—is often considered as a second-order effect, it can be regarded as a ubiquitous phenomenon inside our planet. The origin of seismic anisotropy is manifold. Originally observed for horizontal wave propagation in the upper mantle due to aligned crystals (e.g. Hess 1964), anisotropy can be caused by aligned pore space or cracks (e.g. Crampin 1984), bedding of sediments (e.g. Backus 1962), apparent anisotropy (e.g. Babuška & Cara 1991), convective flow in the Earth's inner core (e.g. Morelli *et al.* 1986; Woodhouse *et al.* 1986; Song 1997), and—as a consequence—provides the connection between the seismic wavefield and internal dynamics in terms of convective flow, strain/stress orientation and their temporal changes. Especially in stratigraphic exploration, information about anisotropic parameters leads to more precise assessments of lithology, fracture density and flow paths for improved oil recovery (Corrigan *et al.* 1986; Wang 2002; Helbig & Thomsen 2005).

Seismology is classically built on the observation of at most three ground-motion components of displacement (velocity or acceleration). However, the theory of deformation of a fully elastic medium not only includes three components of translation but also three components of rotations and six components of strain (e.g. Aki & Richards 2002; Stein & Wysession 2002; Cochard *et al.* 2006). With the recent advent of portable rotation sensing technologies fit for broad-band observations (e.g. Bernauer *et al.* 2012, 2018; Yuan *et al.* 2020) as well as the emerging potential of (longitudinal) strain measurements using distributed acoustic sensing (DAS, e.g. Lindsey & Martin 2021) entirely new observational concepts for all fields of seismology, applied seismics and engineering are possible.

It is well known that multicomponent ground-motion observations provide the opportunity to estimate wavefield properties (e.g. phase velocities and propagation direction) otherwise only accessible through seismic array measurements (e.g. Pancha *et al.* 2000; Igel *et al.* 2005, 2007; Cochard *et al.* 2006; Bernauer *et al.* 2009; Fichtner & Igel 2009; Hadziioannou *et al.* 2012; Edme & Yuan 2016; Sollberger *et al.* 2017, 2020). So far, theoretical and field studies of rotational motions were mainly based on the assumption of isotropic elastic media. Exceptions are the analysis by Pham *et al.* (2010), investigating the rotational components of *P* waves in anisotropic media and the theoretical study by Tang & Fang (2021) developing forward models in transversely isotropic media for six-component ground motions.

Single-point wavefield analysis can be an important methodology in situations in which seismic arrays are difficult or impossible to realize. This applies to boreholes, the ocean bottom, remote areas, volcanoes, cities, or planetary installations. Multicomponent ground-motion observations can play an important role in improving the resolution power for structural and seismic source parameters. Recent examples are the local structural inversion in the context of microzonation (Wassermann *et al.* 2016; Keil *et al.* 2020), moment

*Now at: Department of Earth Sciences, ETH Zurich, Switzerland

tensor inversion (e.g. Donner *et al.* 2018), or planetary applications (e.g. Bernauer *et al.* 2020).

In this study, we aim at extending the multicomponent wavefield (or polarization) analysis (e.g. Sollberger *et al.* 2017, 2020) to anisotropic elastic media. As a first step we solve the forward problem of calculating waveforms for quasi-*P* (qP) and quasi-*S* waves (qS) analytically assuming plane-wave propagation in unbounded homogeneous anisotropic media. In practical terms this corresponds to a highly simplified application of multicomponent downhole recordings at depth. We seek an answer to the question whether at a single measurement point anisotropic wave velocities can be estimated from multicomponent ground-motion observations and under what conditions all anisotropic elastic tensor components can be determined.

The paper is structured as follows: after this Introduction, we present the basic plane-wave theory for wave propagation in anisotropic media and displacement, rotation and strain observables. Based on this formulation we pose an inverse problem strategy for the elastic tensor. We apply this strategy to noise-free, and noisy synthetic multidirectional plane-wave observations. The initial six-component analysis is extended by adding one longitudinal strain component (along the virtual borehole, a common experimental setup), investigating the improvement in elastic tensor recovery. Finally, the results are discussed and an outlook to possible further studies is given.

2 THEORY

2.1 Seismic translation, rotation and strain

2.1.1 Plane waves

Displacement $\mathbf{u}$ and acceleration $\ddot{\mathbf{u}}$ of a plane harmonic seismic wave propagating in a fully elastic homogeneous medium can be described with following relationships depending on location $\mathbf{x}$ and time t

$$\mathbf{u}(\mathbf{x},t) = A\mathbf{n}\exp\left[i\omega\left(t-\frac{\boldsymbol{\nu}\cdot\mathbf{x}}{v}\right)\right] \tag{1}$$

$$\ddot{\mathbf{u}}(\mathbf{x},t) = \partial_t^2\mathbf{u} = -\omega^2 A\mathbf{n}\exp\left[i\omega\left(t-\frac{\boldsymbol{\nu}\cdot\mathbf{x}}{v}\right)\right] \tag{2}$$

where A is the ground displacement peak amplitude, $\mathbf{n}$ is the unit translational polarization vector, ω is the angular frequency, $\boldsymbol{\nu}$ is the unit propagation direction vector, v is the phase velocity and i is the imaginary unit.

Rotation rates $\dot{\Omega}$ are derived from translational motions by taking half the curl of the velocity field (e.g. Igel *et al.* 2005; Cochard *et al.* 2006):

$$\dot{\Omega}(\mathbf{x},t) = \frac{1}{2}\nabla\times\partial_t\mathbf{u} = \frac{A\omega^2}{2v}\begin{pmatrix}\nu_2 n_3-\nu_3 n_2\\ \nu_3 n_1-\nu_1 n_3\\ \nu_1 n_2-\nu_2 n_1\end{pmatrix}\exp\left[i\omega\left(t-\frac{\boldsymbol{\nu}\cdot\mathbf{x}}{v}\right)\right]. \tag{3}$$

Strainmeters measure changes in length scale. Assuming that the direction of measurement is along the vertical axis x_3 then the corresponding strain rate results in

$$\dot{\epsilon}_{33}(\mathbf{x},t) = \partial_t\partial_3 u_3 = \frac{A\omega^2\nu_3 n_3}{v}\exp\left[i\omega\left(t-\frac{\boldsymbol{\nu}\cdot\mathbf{x}}{v}\right)\right]. \tag{4}$$

2.1.2 Material properties

Velocity v and polarization $\mathbf{n}$ are connected to the material properties with the eigenproblem posed by the Kelvin–Christoffel equation (see e.g. Musgrave 1970; Van Buskirk *et al.* 1986)

$$(\Gamma-\rho v^2\mathbf{I}_3)\cdot\mathbf{u} = 0 \tag{5}$$

with the (3×3) identity matrix $\mathbf{I}_3$, the material density ρ (isotropic constant) and the Kelvin–Christoffel matrix Γ. The Kelvin–Christoffel matrix is symmetric and a projected representation of the elastic tensor along the propagation direction:

$$\Gamma = \mathbf{L}\cdot\mathbf{C}\cdot\mathbf{L}^T \tag{6}$$

with

$$\mathbf{L} = \begin{pmatrix}\nu_1 & 0 & 0 & 0 & \nu_3 & \nu_2\\ 0 & \nu_2 & 0 & \nu_3 & 0 & \nu_1\\ 0 & 0 & \nu_3 & \nu_2 & \nu_1 & 0\end{pmatrix} \tag{7}$$

and the symmetric elastic tensor $\mathbf{C}$ with its 21 independent parameters

$$\mathbf{C} = \begin{pmatrix}C_{11} & C_{12} & C_{13} & C_{14} & C_{15} & C_{16}\\ & C_{22} & C_{23} & C_{24} & C_{25} & C_{26}\\ & & C_{33} & C_{34} & C_{35} & C_{36}\\ & & & C_{44} & C_{45} & C_{46}\\ & \mathbf{sym.} & & & C_{55} & C_{56}\\ & & & & & C_{66}\end{pmatrix} \tag{8}$$

In this study, we derive an inversion scheme for the elastic tensor $\mathbf{C}$. Materials behaving similarly in all directions are called *isotropic* and corresponding elastic tensor have two independent parameters. Whenever the amount of independent parameters exceeds two, the material behaves *anisotropically* since its characteristics (e.g. wave velocities) depend on the propagation direction. *Vertical transverse isotropy* (VTI)—symmetry is most commonly utilized in seismic studies, since it addresses wave propagation in horizontally layered rock. Directional dependencies of such a medium are attributed to just one angle, which is the angle of incidence. VTI materials are hexagonal with a vertically aligned symmetry axis and have five independent elastic parameters (Love 1892).

$$\mathbf{C}_{VTI} = \begin{pmatrix}C_{11} & C_{11}-2\cdot C_{66} & C_{13} & 0 & 0 & 0\\ & C_{11} & C_{13} & 0 & 0 & 0\\ & & C_{33} & 0 & 0 & 0\\ & & & C_{55} & 0 & 0\\ & \mathbf{sym.} & & & C_{55} & 0\\ & & & & & C_{66}\end{pmatrix} \tag{9}$$

When a material is perpendicularly fractured to its stratification, the elastic tensor relates to orthorhombic symmetry (Schoenberg & Helbig 1997). Hence, this symmetry system has recently gained importance in local seismic tomography. Orthorhombic behaviour is characterized by nine independent elastic parameters. Assuming the symmetry directions are aligned with the coordinate axes, the representation of the elastic tensor is as follows:

$$\mathbf{C}_{\text{ortho}} = \begin{pmatrix}C_{11} & C_{12} & C_{13} & 0 & 0 & 0\\ & C_{22} & C_{23} & 0 & 0 & 0\\ & & C_{33} & 0 & 0 & 0\\ & & & C_{44} & 0 & 0\\ & \mathbf{sym.} & & & C_{55} & 0\\ & & & & & C_{66}\end{pmatrix}. \tag{10}$$

Wave propagation in a fully elastic medium follow the eigenproblem described in eq. (5). The eigenvectors of the Kelvin–Christoffel matrix are the polarizations $\mathbf{n}$ and corresponding eigenvalues are

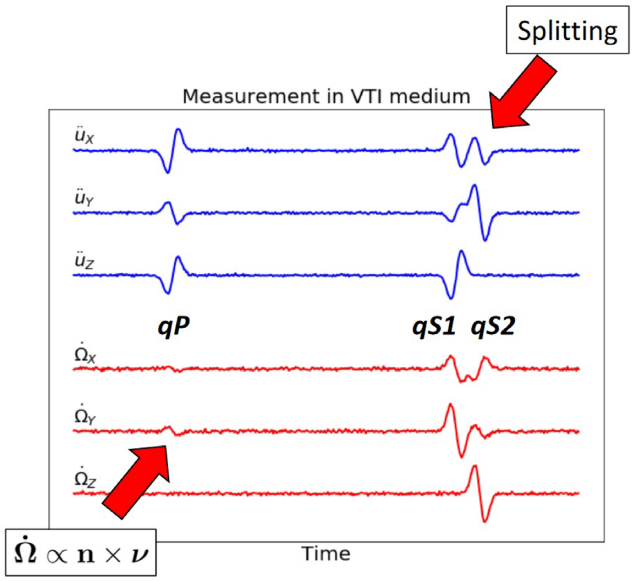

Figure 1. Exemplary synthetic six-component borehole seismogram inside a VTI-medium (Taylor Sandstone) with acceleration $\ddot{\mathbf{u}}$ and rotation rate $\dot{\Omega}$ during the arrivals of qP, qS1 and qS2 waves. Two important properties of anisotropic media are evident, namely the splitting of shear waves and the rotation of the qP wave. Portrayed measurements are perturbed with an SNR of 30.

the product of velocity squared and density. In general, there are three non-degenerate eigenvalues and hence there are three distinctly propagating wavefields denoted by qP, qS1 and qS2 (see e.g. Crampin 1977). This is not the case under isotropic conditions and also specific directions—called singularities—in general anisotropic media in which qS1 and qS2 travel at the same velocity. Separate arrivals of those waves are called *shear wave splitting*. Another general solution is that the polarizations are neither necessarily parallel nor perpendicular to the propagation direction. So, in general, all body waves (including qP waves) exhibit rotations (Pham *et al.* 2010). Phenomena attributed to anisotropy are summarized and visualized in Fig. 1. The symmetry of the Kelvin–Christoffel matrix ensures that the set of body-wave polarization vectors form an orthonormal basis. Further, Γ can be diagonalized with its eigenvectors and eigenvalues.

$$\Gamma = \begin{pmatrix} . & . & . \\ \mathbf{n}_1 & \mathbf{n}_2 & \mathbf{n}_3 \\ . & . & . \end{pmatrix} \begin{pmatrix} \rho v_1^2 & 0 & 0 \\ 0 & \rho v_2^2 & 0 \\ 0 & 0 & \rho v_3^2 \end{pmatrix} \begin{pmatrix} . & . & . \\ \mathbf{n}_1 & \mathbf{n}_2 & \mathbf{n}_3 \\ . & . & . \end{pmatrix} \tag{11}$$

Therefore, with known density, estimated wave velocities and corresponding polarizations, it is possible to reconstruct the Kelvin–Christoffel matrix.

2.2 Inversion scheme—anisotropic elastic tensor estimations using 6C observations

When examining eq. (6), one can recognize the usual constituents for a linear inverse problem of the pattern

$$\mathbf{d} = \mathbf{G}\mathbf{m} \tag{12}$$

where $\mathbf{d}$ is the data vector, $\mathbf{m}$ the model that is inverted for and $\mathbf{G}$ the forward operator composed of propagation directions. In the inverse problem at hand, the Kelvin–Christoffel matrix resembles the observable, the model are the 21 elastic parameters and the forward operator depends on the propagation direction. The model $\mathbf{m}$ that minimizes squared errors can be found with

$$\mathbf{m} \approx (\mathbf{G}^T\mathbf{G})^{-1}\mathbf{G}^T\mathbf{d} \tag{13}$$

To unambiguously solve for the model vector, the Kelvin–Christoffel matrices of at least six events with different propagation directions have to be calculated (Van Buskirk *et al.* 1986). Similar approaches for elastic tensor inversions have been investigated in the context of walkaway vertical seismic profiles by Dewangan & Grechka (2003) and Asgharzadeh *et al.* (2013), a situation where sources moved progressively further away while receivers remain at fixed locations. In the following, we explain how propagation directions and wave velocities can be estimated from six-component (translations and rotations) measurements at a single borehole station.

2.3 Propagation direction estimation

We assume that the propagation direction is constant for all body wave phases originating from one event. Since the method should be valid for any symmetry system, the polarization of the *P* wave does not act as an ideal indicator of the propagation direction. Instead, the propagation direction can be estimated through the inspection of the rotational components. Examining eq. (3) uncovers that rotational polarizations $\mathbf{r}_j$ induced by wave type j (either qP, qS1 or qS2) are perpendicular to both their respective translational polarization and the propagation direction (Pham *et al.* 2010).

$$\mathbf{r}_j \propto \nu \times \mathbf{n}_j \tag{14}$$

Since $\boldsymbol{\nu}$ is a constant, the combined rotational motion of all phases is bound by the plane defined through its orthogonality to the propagation direction. This 2-D vector space is unambiguously determined when at least two of its (linearly independent) vectors are known. Thus, the propagation direction can be retrieved by the cross-product of two of those vectors ($i \neq j$, $i, j \in \{$qP, qS1 or qS2$\}$):

$$\nu = \frac{\mathbf{r}_i \times \mathbf{r}_j}{||\mathbf{r}_i \times \mathbf{r}_j||} = \frac{(\nu \times \mathbf{n}_i) \times (\nu \times \mathbf{n}_j)}{||\mathbf{r}_i \times \mathbf{r}_j||} \tag{15}$$

The applicability of eq. (15) relies on measuring at least two distinctly polarized rotational signals because then rotational polarization vectors $\mathbf{r}_i$ and $\mathbf{r}_j$ can be estimated from the measurements. Therefore, this method cannot be applied in isotropic materials since there is only one *S*-wave arrival and the *P* wave does not carry a rotational signal. Of course, in this case, one would simply identify the *P*-wave's polarization or the vector perpendicular to both translational and rotational motions of the *S* wave as the propagation direction.

Problems also arise in anisotropic media. Along singular directions, only one rotational signal can be recorded from the shear waves. If the qP-wave rotation is sufficiently pronounced, it is possible to compare qP and qS rotations to deduce the propagation direction. However, rotations on Earth are usually much smaller for qP waves than for qS waves and therefore such results may come with a significant error. Ideally, shear waves appear split and the propagation direction estimation is based on their measured rotations.

The forward operator $\mathbf{G}$ in eq. (13) embodies all considered propagation directions and can therefore be interpreted as an indication how the event distribution effects the inversion. Values of $(\mathbf{G}^T\mathbf{G})^{-1}$—given its solution is unique and exists—serve as a preliminary hint at the geometric resolution of the elastic tensor without considering the quality of velocity estimations. For example, if signals from all events arrive near a horizontal angle, the bulk

modulus in the vertical direction is expected to be poorly resolved compared to those in horizontal directions since this parameter is mainly determined by qP waves arriving at close to vertical angles. Such preliminary assessments of expected resolution can be carried out by inspecting the quantities of $(\mathbf{G}^T\mathbf{G})^{-1}$.

2.4 Velocity estimation

The propagation direction must be determined prior to velocity estimations. Since the six-component measurements fully capture translational and rotational motions in three spatial directions, the seismograms can be rotated into radial (R), transversal (T) and vertical (V) directions. The propagation direction coincides with the radial axis such that $\boldsymbol{\nu} = (1, 0, 0)^T$. Within this new reference frame, accelerations and rotation rates simplify to:

$$\begin{aligned}\ddot{\mathbf{u}}(\mathbf{x}, t) &= -\omega^2 A \begin{pmatrix} n_R \\ n_T \\ n_V \end{pmatrix} \exp\left[i\omega\left(t - \tfrac{\nu\cdot\mathbf{x}}{v}\right)\right] \\ \dot{\Omega}(\mathbf{x}, t) &= \tfrac{A\omega^2}{2v} \begin{pmatrix} 0 \\ -n_V \\ n_T \end{pmatrix} \exp\left[i\omega\left(t - \tfrac{\nu\cdot\mathbf{x}}{v}\right)\right] \end{aligned} \tag{16}$$

The entirety of rotational motion is acquired by transverse and vertical axes. The ratio between translational and rotational amplitudes on transversal and vertical components leads to an expression for the phase velocity.

$$v = \frac{1}{2}\frac{\sqrt{\ddot{u}_T^2 + \ddot{u}_V^2}}{\sqrt{\dot{\Omega}_T^2 + \dot{\Omega}_V^2}} \tag{17}$$

During the derivation of eq. (17), no assumption about wave type was made. In fact, this velocity estimation works for qP, qS1 and qS2 waves equivalently. Shear wave velocity estimation with comparable ratios between translational and rotational signals were introduced before (see e.g. Cochard *et al.* 2006), however, to the best of our knowledge, never expanded towards qP waves. By further analysing eq. (17), it becomes apparent that the feasibility of the qP-wave velocity estimation relies on the anisotropic properties of the material; Under isotropic conditions, nominator and denominator of eq. (17) both acquire the value zero—or when considering noise, tiny values—and therefore the result of the ratio bears no relevant physical meaning. Even before consulting the outcomes of synthetic tests, we can hence already expect that the weak link of the 6C-inversion scheme lies within the estimation of the qP-wave velocity. Therefore, after the following section, a seven-component scheme is presented that includes a strainmeter and enables an alternative way to extract qP-wave velocities.

3 SYNTHETIC TESTS

3.1 Experimental setup

To test the theory of inversion for elastic tensors developed in this study, results from synthetic tests are presented in the following. A hypothetical six-component sensor is placed in a borehole in a homogeneous medium. Events are randomly distributed around this receiver and source kinematics are isotropic in *S* and *P*. Body waves travel from source to receiver in plane harmonic waves. The analytical solution to this problem is found with the Kelvin–Christoffel equation (see eq. 5). To make the scenarios more realistic, the analytical recordings are perturbed by some noise. We choose white Gaussian noise. Hence, the noise level is consistent among all frequencies and is driven by a single input parameter—the signal-to-noise ratio (SNR). Conveniently, since we simulate uniform amplitudes for all body waves, the SNR does not deviate between the different wave types. This hypothetical situation is illustrated in a sketch in Fig. 2.

The rock *Taylor Sandstone* serves as the medium in all of the tests. Its anisotropic properties are adapted from a real-world example and belongs to the group of VTI materials. It was selected from the catalogue listed in Thomsen (1986) because of its moderate strength in anisotropy and the existence of an *S*-wave singularity (at ca. 42.5°). *S*-wave singularities appear in certain directions of anisotropic media where both *S* waves travel at the same velocity, that is, an angle at which eigenvalues of the Kelvin–Christoffel matrix are degenerate. qP rotations are strongest around 58°. VTI symmetry is at the forefront when dealing with anisotropy in seismological studies and therefore we also utilize it here. Note however, that at no point during the inversion scheme an assumption about the symmetric characteristics of the material was made, and hence we aim at resolving all 21 elastic parameters simultaneously—the inversion treats the rock as if it was triclinic. To underline this statement, the inversion scheme is further demonstrated on the orthorhombic material *phenolic CE*. It is an industrial laminate that has been used in physical seismic modelling studies (Cheadle *et al.* 1991). Details about the materials in this study are provided in Appendix A.

At first, we take a look at the individual building blocks of the inversion scheme, that is, estimations of propagation direction and velocities. Afterwards, we examine how the precision and accuracy of the determined elastic tensor parameters vary depending on the SNR.

3.2 Results of propagation direction estimation

The propagation direction of an incoming event is determined by comparing rotational motions that are induced by split shear waves. Whether or not two separate shear wave arrivals are distinguishable depends on source–receiver distance, difference in velocity, SNR, wave frequency, sampling rate and material properties. Whenever qS waves arrive inseparably at the receiver, the propagation direction cannot be uniquely determined with the method that follows. Commonly, at least within most realistic applications on Earth, qP-wave polarizations are expected to point roughly into the direction of propagation. Therefore, we estimate the propagation direction of events with non-split shear waves in the seismometer by simply adapting it as the polarization of qP waves. Note that in an anisotropic medium, qP-polarization and propagation direction are not necessarily parallel even if qS waves are not split.

To illustrate the performance of the method (Fig. 3), the error behaviour as a function of SNR of the rotational components for four incident angles is analysed; *Horizontal* and *60°* produce seismograms with split shear waves, at 43° (*Vicinity of singularity*) shear waves are only split for high-quality measurements, and *vertical* qS waves are never separated.

The average errors monotonously decrease for increasing SNR, displaying convergent behaviour. We find that for split qS waves, an SNR of 10 conforms to average errors of around 1° and at an SNR of 1 (=0 dB) the error is below 5°. Expected errors are lower in vertical direction since we simulate translational components to be of better quality than rotational components. This angle basically

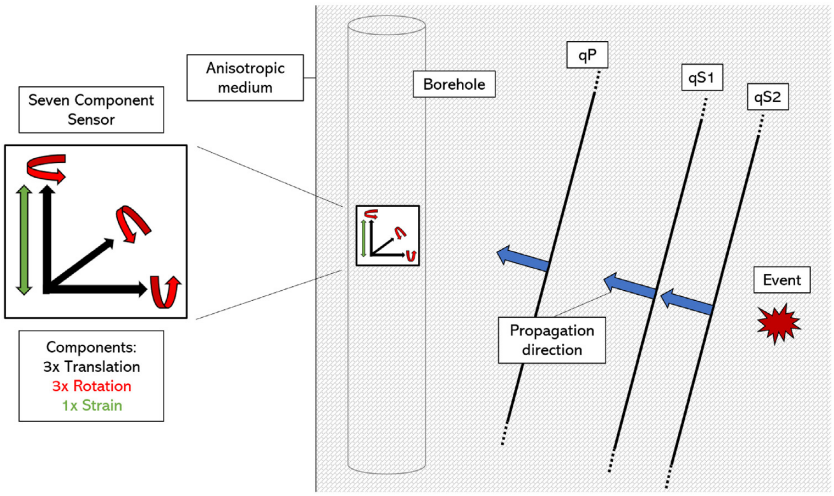

Figure 2. Schematic overview of the hypothetical setting. The seven-component sensor with three translational, three rotational and one strain component is located inside a borehole. The surrounding material is homogeneously anisotropic. Induced events radiate three types of waves (qP, qS1 and qS2) and they arrive at the receiver in planar form. The propagation direction is uniform for body waves.

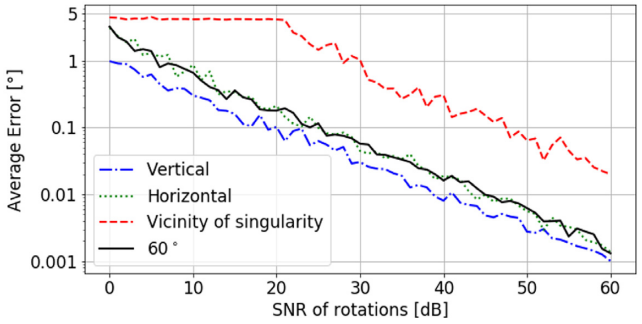

Figure 3. Error behaviour of propagation direction determination for selected angles in a VTI medium (Taylor Sandstone). Errors for each sampled SNR are derived from 30 different noise realizations of the same event. The average angular deviation between the estimated and true propagation directions are displayed. SNR of translations is 10 dB higher compared to the portrayed SNR of rotations. At an inclination of approximately 43°, Taylor Sandstone exhibits an *S*-wave singularity. At vertical incidence, shear wave splitting is absent and thus qP-polarization is always utilized for the estimation. Horizontal events and those with an angle of incidence of 60° are suitably separated from singularities to allow an application of the method with rotational polarizations.

behaves isotropically which is why the qP-polarization serves as an indication for the propagation direction.

The method commits a systematic error close to the singularity. At this angle, the analytical solutions for qP-polarization and propagation direction are nearly off by 5° which corresponds to the error displayed by the graph. When the SNR exceeds 20 dB, the split nature of the shear waves gets noted and a convergent trend can be observed from there on. The issue with the utilization of qP-polarization as an estimate for the propagation direction is that the residual vectors are not randomly orientated in space. This introduces non-normally distributed errors for velocity estimations and for the elastic tensor inversion.

3.3 Results of velocity estimation

After rotating the six-component measurements into radial, transversal and vertical directions—following the estimation of propagation direction—ratios of translational and rotational signals allow an assertion of the phase velocity, as stated in eq. (17). This is one of the key advantages of 6C observations. For a proper evaluation of velocities, a short time window around the respective qP-, qS1- and qS2-wave arrivals is considered. Estimates are therefore attained by means of an average of the ratio over multiple data samples.

We display relative standard deviations of velocity estimations v_{est} around the true velocity v_{true} based on $N = 50$ random noise realizations of the same situation, that is,

$$\sigma_{\text{relative}} = \frac{\sqrt{\frac{1}{N}\sum_i^N (v_{\text{est},i} - v_{\text{true}})^2}}{v_{\text{true}}} \times 100\,\text{per cent}\ . \tag{18}$$

First, relative standard deviations are examined under varying incidence angles. Fig. 4 contains two VTI materials in order to visualize the material dependency of the method. Both shear wave velocity estimations are equally well resolved and do not depend on the incidence angle. At an SNR of 100, white gaussian noise causes an expected deviation of less than 1 per cent for qS-wave velocities.

The reliance on material properties becomes apparent when inspecting the errors for qP-wave velocities. Both portrayed VTI materials have preferable angles of incidence where better constrained results are obtained and inclinations where a velocity estimation is infeasible. For the chosen examples, and anticipated for most rocks found on Earth, the standard deviations are significantly higher for qP-wave velocities compared to qS-wave velocities. This behaviour can be attributed to less pronounced rotations induced by qP waves. In fact, the driving force behind the resolution of qP-wave velocities is the angle spanned by propagation direction and qP-polarization, which is supported by analytical results for the respective materials under investigation.

To further illustrate the dependency on material properties, the next experiment is conducted on altered elastic tensors of Taylor Sandstone, giving the maximal *P* anisotropy as a variable. The adapted synthetic materials are derived from changing all Thomsen parameters simultaneously in a linear manner. This ensures that the highest resolution remains at the same angle, which is at 58° and therefore, Fig. 5 shows results for this specific angle only.

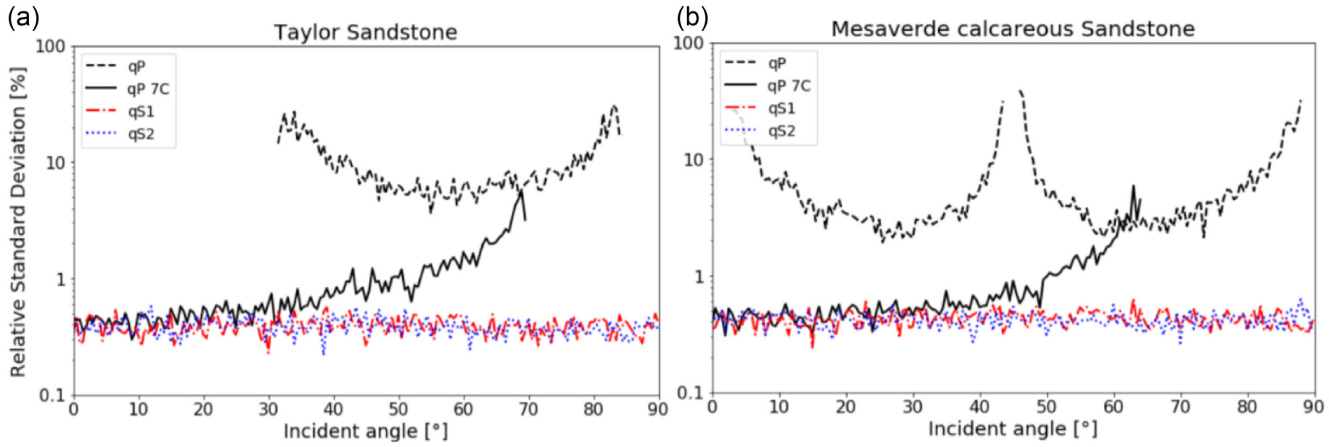

Figure 4. Relative standard deviations of velocity estimations from 6C measurements and qP-wave velocity estimation from 7C measurements depending on the incident angle in VTI media (Taylor Sandstone and Mesaverde calcareous Sandstone, both from Thomsen 1986) at SNR of 100. The 7C analysis is explained in detail in Section 4. Relative standard deviations are normalized by the true velocity to ensure comparability between different materials (see eq. 18). Standard deviations are based on 50 repetitions for each sampled incident angle.

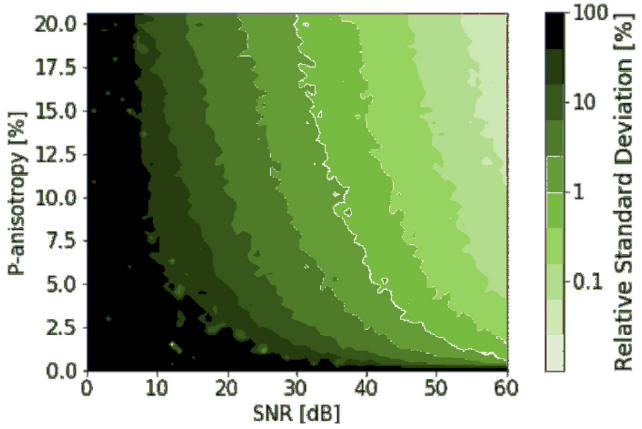

Figure 5. Relative standard deviation of rotation-derived P-wave velocities with respect to SNR and P anisotropy ($\max_\theta v_p(\theta)/\min_\theta v_p(\theta) - 1$) at an angle of incidence of 58°. The synthetic materials have been produced by linearly changing the values of the Thomsen parameters of Taylor Sandstone (Thomsen 1986). The default Taylor Sandstone has a P anisotropy of 10 per cent. Standard deviations based on 50 repetitions for each material-SNR pair.

Independent of SNR, the qP-wave velocity cannot be estimated from 6C measurements if the medium under investigation is isotropic, which was expected from theory. The higher the quality of the data, the less anisotropy is required to obtain a reasonable estimate of the qP-wave velocity. Below an SNR of 10, the qP-wave velocities cannot be resolved for media up to twice the P anisotropy of Taylor Sandstone.

3.4 Results of elastic tensor estimation

After discussing the methods to extract propagation direction and wave velocities at a six-component borehole receiver, we have all the ingredients needed for an elastic tensor estimation.

To illustrate the validity of the method, noiseless measurements are evaluated first on the basis of two exemplary media. For each elastic tensor inversion, the synthetic six-component recordings of 25 randomly distributed events are analysed. Results are shown in Fig. 6. Portrayed error bars visualize one standard deviation based on 500 repetitions of the experiment. It is evident that each of the 21 elastic parameters is precisely recovered. Indeed, the inversion scheme yields results up to machine precision. This is true for both hexagonal and orthorhombic symmetries and, in general, entirely independent of the investigated symmetry system.

In the following, it is investigated how sensitive the resolution reacts to imperfections in the recordings. The results for an SNR of 100 are presented in Fig. 7 as histograms. The resolution of each individual parameter depends on its position in the elastic tensor. Standard deviations are lowest for elastic parameters $\mathbf{C}_{4:6,4:6}$ because this section of the tensor is mostly sensitive to shear wave velocity estimations. Anisotropic behaviour of qS waves can be confidently resolved since C_{55} is distinctly different from C_{66}. Therefore, the medium can definitely be classified as non-isotropic. Elastic parameters $\mathbf{C}_{1:3,1:3}$ are significantly less well resolved. These parameters are mostly sensitive to the qP-wave velocity estimate and it was shown before that rotations are not necessarily suited for this task. A P anisotropy cannot be observed since the Gaussian curves of histograms of C_{11}, C_{22} and C_{33} overlap significantly. Moreover, there seems to be a tendency to underestimate these entries of the elastic tensor. This results from difficulties in determining qP-wave velocities for some directions with hardly any rotations in qP. It could be argued that no real information was gathered since educated guessing of elastic parameters could have probably lead to similar results than those obtained by $\mathbf{C}_{1:3,1:3}$.

The intermediate parameters of $\mathbf{C}_{1:3,4:6}$ exhibit standard variations greater than $\mathbf{C}_{4:6,4:6}$ and lower than $\mathbf{C}_{1:3,1:3}$. The estimates are consistently close to zero, as they are expected to be. Nevertheless, due to the usage of a tilted VTI medium, some should be distinctly non-zero, however this cannot be resolved.

The resolution of the inversion of the elastic tensor based on a joint translational and rotational measurement leaves a lot to be desired as many crucial attributes of the elastic tensor cannot be resolved for an SNR of 100, which is already unrealistically high. The main cause can be assigned to the poorly resolved qP-wave velocity estimation. And this is perfectly reasonable since qP waves are predominantly divergent and therefore induce little to no rotations. The elastic tensor estimation at a single station could be improved if the instrument actually exploited the volume changing properties of qP waves. This can be measured by a strainmeter, which directly captures changes in length scales. In the following, we upgrade the

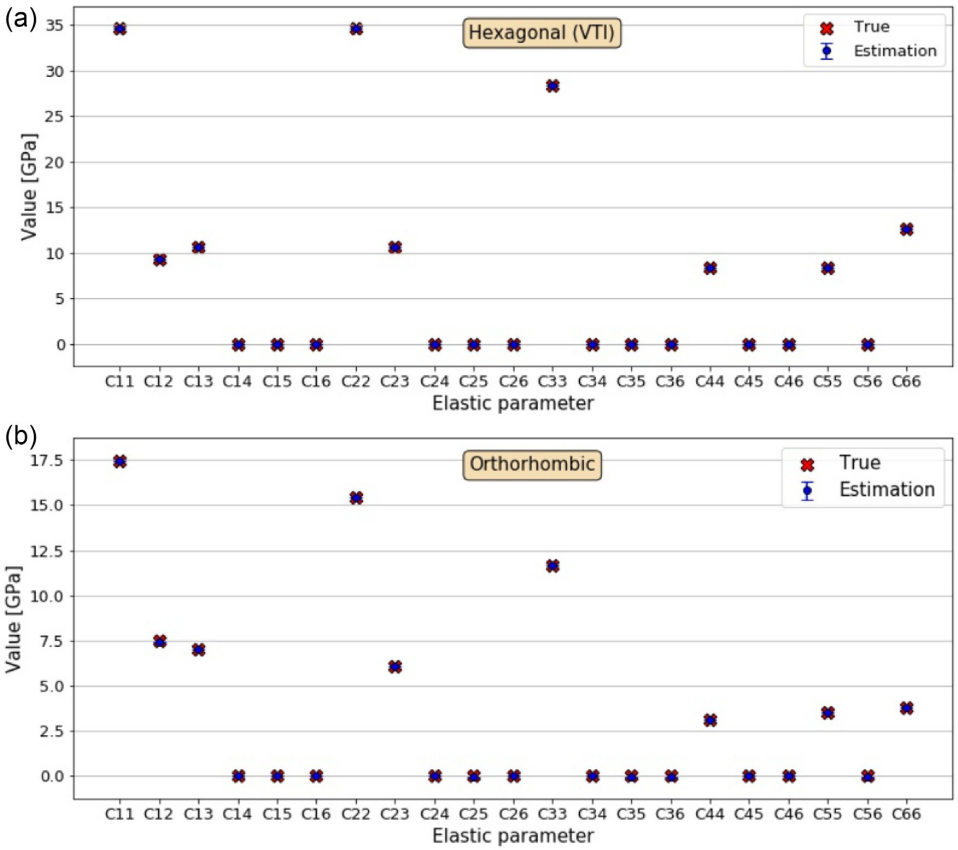

Figure 6. Results of 500 repetitions of the elastic tensor inversion based on noise-free six-component recordings for 25 randomly located events in (a) VTI symmetry (Taylor Sandstone) and (b) orthorhombic symmetry (Phenolic CE). True elastic parameter values are indicated by red crosses, blue dots illustrate the mean of estimated parameters and error bars signal one standard deviation. In this perfect noise-free case, the true values are always resolved which shows the validity of the elastic tensor inversion method.

six-component receiver to a seven-component receiver and carry out the inversion scheme once again. Propagation direction and qS-wave velocities are extracted the same way as before with rotational components while qP-wave velocities can be retrieved alternatively.

4 7C ANALYSIS

In this section we investigate the potential of one additionally observed strain component (longitudinal along the virtual borehole), thus 7C, to improve the resolution of the inverted anisotropic elastic constants.

4.1 qP-wave velocity estimation with strain

Observed strain rates induced by plane waves are inversely proportional to the wave velocity (see eq. 4). Formulating an adequate ratio with the acceleration component, an expression for the phase velocity v can be obtained (formula comparable to e.g. Bernauer *et al.* 2012).

$$v = \frac{\dot{\epsilon}_{33}}{\ddot{u}_3} \nu_3 = \frac{\dot{\epsilon}_{33}}{\ddot{u}_3} \cos\theta \tag{19}$$

Here, $\dot{\epsilon}_{33}$ is the strain rate gauged in the strainmeter oriented along axis 3, $\ddot{u}_3$ is the observed acceleration and ν_3 is the portion of the estimated unit propagation direction vector in this direction. Another way to assess the influence of the propagation direction lies with the cosine of an angle θ that describes the opening angle between strainmeter and propagation direction. For a vertically oriented strainmeter, this angle coincides with the angle of incidence.

4.2 qP-wave velocity estimation with strain—results

In theory, eq. (19) can be applied to obtain any body phase velocity. In the context of this study, it is only implemented to obtain a superior qP-wave velocity estimate. Rotational components are still utilized to acquire qS-wave velocity estimates. The superiority of constraining qP-wave velocities with a strainmeter is illustrated in Fig. 4. In contrast to the rotation-derived qP-wave velocities, the strain-based method's resolution is independent of material properties. Hence, anisotropic features are not mandatory for an assessment of a medium's qP-wave velocity. The expected errors depend rather on the geometric outline of the problem (i.e. the opening angle between strainmeter and propagation direction). For near vertical arrivals, relative standard deviations of the qP-wave velocities are of the same order of magnitude as for qS-wave velocities. With an increasing opening angle between strainmeter and propagation direction, the capability of the strainmeter to measure the *P* waves signal decreases until the noise level prevents a reasonable estimation for too shallow arrivals.

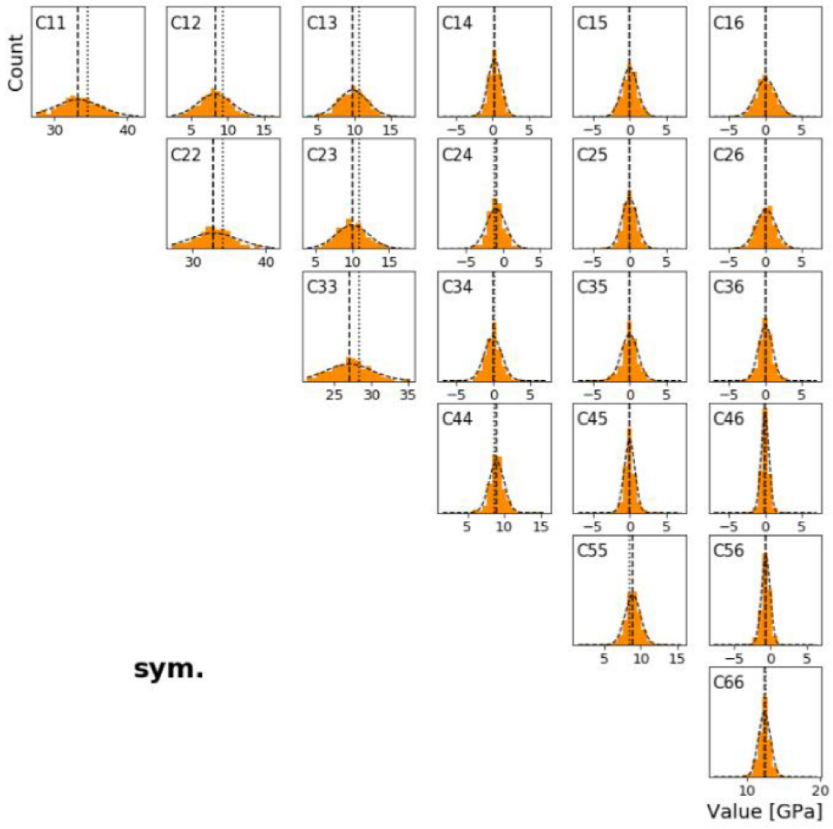

Figure 7. Histograms for 500 repetitions of the elastic tensor inversion at an SNR of 100 in a 10°-tilted Taylor Sandstone. The arrangement of histograms mirrors the appearance of the Voigt-notation elastic tensor. True values are indicated by dotted vertical lines. Dashed vertical lines are the mean value of the inversion and the Gaussian curves are maximum-likelihood solutions. The resolution of elastic parameters depends on the location inside the elastic tensor.

4.3 7C Inversion results

The effects of an improved qP-wave velocity estimation concept through the addition of a strainmeter to the 3-D translational and rotational measurements on the elastic tensor estimation can be seen in Fig. 8. Every single one of the 21 elastic parameters is considerably better constrained for the strain inversion scheme. Maybe surprisingly, this is equally valid for parameters $\mathbf{C}_{4:6,4:6}$ even though we established that those are mainly responsible for shear wave velocities. However, qP-wave velocities are sensitive to the entire elastic tensor and therefore, in return, the improved qP-wave velocity estimates influence all parameters, even those we mostly associate with shearing motion. Rotation-based results for this SNR are poor for parameters $\mathbf{C}_{1:3,1:3}$, while the strain-method captures them with considerably higher resolution. *P*-wave velocities can confidently be resolved to depend on the direction since the standard deviations of parameters C_{22} and C_{33} do not overlap. This is not true for the rotation-derived elastic tensor where it is also not possible to distinguish between any of the parameters $\mathbf{C}_{1:3,4:6}$. For isotropic and VTI media, those entries are expected to be zero. With the seven-component setup and at this SNR, some parameters, especially C_{24} in this instance, are clearly non-zero. Therefore, when analysing the results of the strain-derived elastic tensor, the material cannot only be classified as strongly anisotropic for *P* and *S* waves, but the popular symmetry system VTI can also be excluded. Assuming that the underlying symmetry system is hexagonal (with an arbitrarily oriented symmetry axis), this train of thought leads to an interesting question: is it possible to derive the orientation of the symmetry axis for the estimated elastic tensor?

4.4 Recovery of the symmetry axis

The elastic tensor inversion scheme presented in this study excludes *a priori* assumption of symmetry. As a consequence, we invert for all 21 elastic parameters simultaneously. This enables us to search for a fitting symmetry system inside the estimated elastic tensor after the inversion itself. The tensor can be tested to belong to any symmetry system (and their rotated variations). If a specific symmetry system was selected beforehand, any retrieved parameters during the elastic tensor inversion are forced to replicate this system. Therefore, the orientation information is lost and (most) other symmetry systems are effectively excluded from the model space.

Here, we would like to focus on the recovery of hexagonal symmetries. In contrast to VTI systems, their symmetry axis are not necessarily vertical. Usually the main part of the elastic tensor is given by the hexagonal component followed by other symmetries (including orthorhombic, Browaeys & Chevrot 2004). The symmetry axis of a hexagonal elastic tensor can be determined with a method presented in Abramian *et al.* (2020) that relies on the characterization of specific covariants. Results are shown in Fig. 9. The chosen medium has a symmetry plane that is tilted by 10°. For both inversion schemes, the estimated symmetry axis directions scatter around the true direction. Errors are considerably smaller for the strain scheme. Outliers can be explained in the following: the method by Abramian *et al.* (2020) aims at determining the noiseless elastic tensors symmetry axis. However, because of the elastic tensor estimation based on noisy data, each entry is attached with some degree of error.

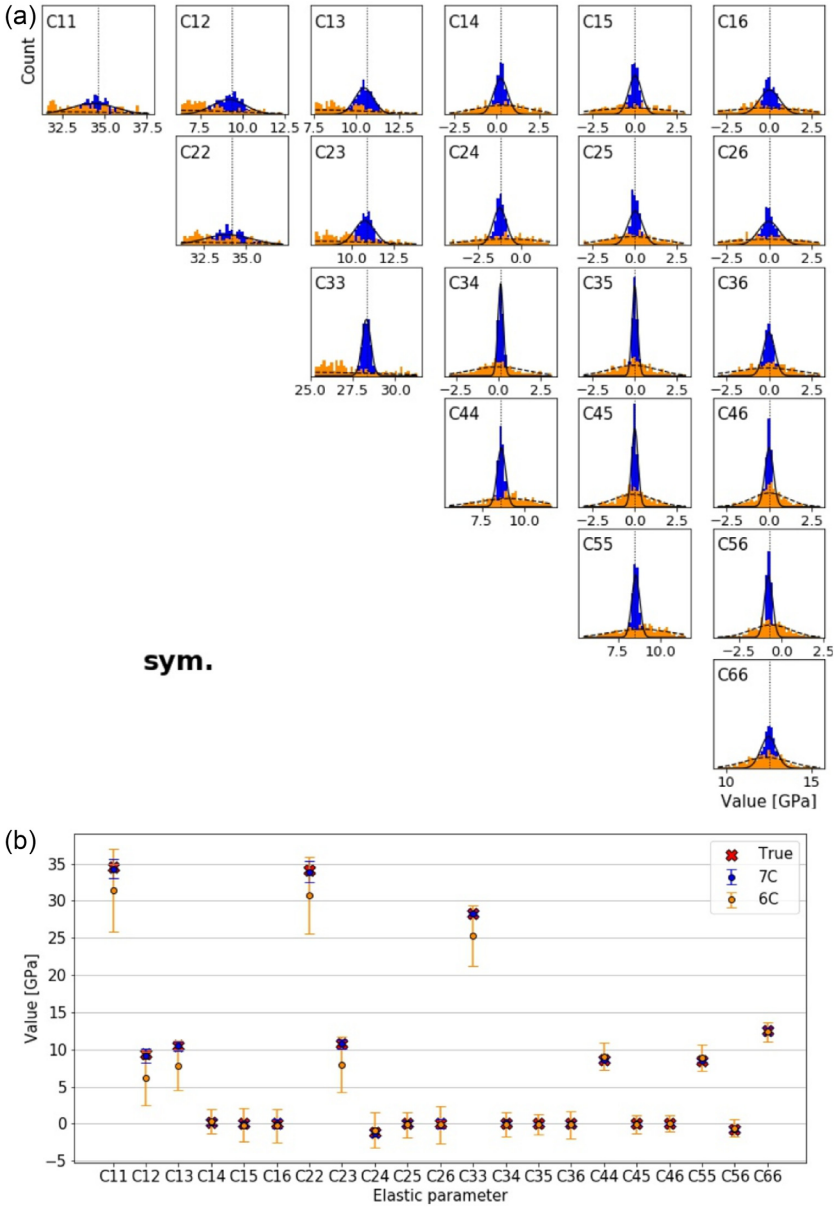

Figure 8. Seven-component inversion for the elastic tensor (dark tone). For this experiment, the setup that went into producing Fig. 7 was repeated with two notable differences. First, *P*-wave velocities are estimated via a vertical strainmeter and second, the SNR of all components is 30 instead of 100. (a) Histograms for all parameters. (b) True values, expected values and one standard deviation of the inversion schemes. For comparison, the results of the six-component inversion scheme (light tone).

5 DISCUSSION

The results in this study indicate that the inversion for the elastic tensor at a single receiver located inside a borehole is—in principle—possible. Theoretically, it is sufficient to deploy a six-component station (three translational and three rotational components) however the lack of a reliable qP-wave velocity estimation derived from rotational motion may render this approach inapplicable. Even though the six-component based elastic tensor inversion may be difficult to implement in practice, it is interesting to note that sufficient information can be drawn from a point measurement to invert for the elastic tensor with its 21 independent constituents from multidirectional wavefields.

When equipping the station with an additional, single-component strainmeter, effectively upgrading it to a seven-component receiver, qP-wave velocities are better constrained and therefore all estimated parameters benefit. In contrast to the rotational approach, the medium is not required to behave anisotropically (curl of qP wave) in order to estimate a qP-wave velocity. Prior to the velocity estimations, the propagation direction must be determined. Since the propagation direction is based on observing rotational signals from split qS waves, it seems essential for the material to be anisotropic for the inversion scheme to function, even though seven-components are analysed. In Appendix B, an alternative approach is presented that enables a derivation of propagation direction from any isolated body wave arrival from seven-component data without the pre-requisite that anisotropy exists in the material. This method has not been applied in this study and therefore not included in the main sections.

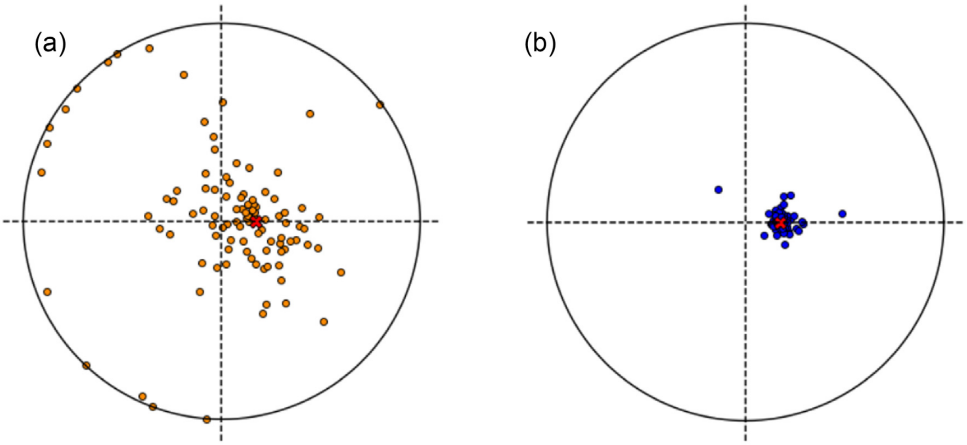

Figure 9. Estimated symmetry axis directions from calculated elastic tensors for 10°-tilted Taylor Sandstone at an SNR of 100 using (a) rotation method and (b) strain method. True symmetry axis indicated by cross. Vertical direction in the centre and the circle indicates horizontal directions.

In practice, the elastic tensor inversion could prove useful since the orientation of subsurface structures, like cracks and/or layers, can be recovered. It is challenging to preserve borehole cores and their exact orientation during the process of drilling, which is why deploying a seven-component station may be more convenient. Various complications accompanied by applying the method to real data are discussed in the following: first and foremost, the question of instrumentation. Translational and strain recorders are commonly placed in boreholes already. The state of the art of rotational receivers does not allow for an instrument that is simultaneously precise and compact, such that it could fit into a borehole. Hopefully, technological advancements in the future lead to reliable seven-component borehole sensors.

Second, the assumption of uniform propagation direction. To enable the reconstruction of the Kelvin–Christoffel matrix from the measurements, the three body waves are required to enter from the same direction. The determination of the propagation direction from rotational measurements also assumes the direction to be constant between split shear waves. This assumption breaks down in strongly heterogeneous media. As was mentioned before, the seven-component receiver provides a way to assign separate propagation directions to each arrival. How this information can be translated into an elastic tensor estimation, skipping the explicit calculation of the Kelvin–Christoffel matrix, is a matter of future research. How a heterogeneous subsurface, that is, a heterogeneous travel path from source to receiver, influences the elastic tensor inversion results is up to debate.

Further, to demonstrate the concept of elastic tensor inversions, it was simplistically assumed that the source dynamic of events are isotropic in *S* and *P*. Energy radiated from realistic sources follow certain patterns (e.g. double couple) and therefore phase amplitudes are different for every event and some phases may not be captured by the station altogether. Future research involving 3-D wave simulations will shed light on what specific effects more complex sources have on elastic tensor inversions.

In theory, the elastic tensor is constrained with six observed events. Of course, more events should be taken into consideration to reduce the effect of noise. In this study, we utilized 25 events of the same magnitude. How many earthquakes need to be observed in a real world setup depends heavily on the specific situation. The most realistic experimental setup to test the method with real observations incorporates active sources. Passively observed earthquake hypocentres cannot be expected to follow a uniform probability distribution in space around the receiver, leading to differences in resolution for each individual elastic parameter.

6 CONCLUSION

This study provides the fundamentals of an elastic tensor inversion performed on data measured at a single borehole receiver. The method requires to map wave velocities of at least six events into different directions. Even though theoretically possible with 3-D translational and rotational measurements, the six-component approach fails due to inferior resolution of qP-wave velocity estimation. With an additional strainmeter, the inversion scheme better constrains all 21 elastic parameters. Interpretations about subsurface structures like cracks and layers and their orientations are feasible by identifying a symmetry system inside the estimated elastic tensor. Before applying the method to real data, more realistic scenarios need to be investigated.

ACKNOWLEDGMENTS

HI is grateful for the support of the Institut de Physique du Globe de Paris, France, for a visiting fellowship in 2019, that kicked off this project. We acknowledge support from the ERC-Adv project ROMY (grant number 339991). Furthermore we acknowledge support through the PIONEERS project funded through the European Union's Horizon 2020 program under grant number 821881.

DATA AVAILABILITY STATEMENT

Python codes for the reproduction of all figures are available on request.

REFERENCES

Abramian, S., Desmorat, B., Desmorat, R., Kolev, B. & Olive, M., 2020. Recovering the normal form and symmetry class of an elasticity tensor, *J. Elasticity,* https://doi.org/10.1007/s10659-020-09784-7.

Aki, K. & Richards, P., 2002. *Quantitative Seismology,* 2nd edn, University Science Books, U.S.

Asgharzadeh, M., Bóna, A., Pevzner, R., Urosevic, M. & Gurevich, B., 2013. Reliability of the slowness and slowness-polarization methods for anisotropy estimation in VTI media from 3c walkaway VSP data, *Geophysics,* **78**(5), WC93–WC102.

Babuška, V. & Cara, M., 1991. *Seismic Anisotropy in the Earth,* Springer, Netherlands.
Backus, G.E., 1962. Long-wave elastic anisotropy produced by horizontal layering, *J. geophys. Res. (1896-1977),* **67**(11), 4427–4440.
Bernauer, F. *et al.*, 2018. blueseis3a: Full characterization of a 3c broadband rotational seismometer, *Seismol. Res. Lett.,* **89**(2A), 620–629.
Bernauer, F. *et al.*, 2020. Exploring planets and asteroids with 6dof sensors: Utopia and realism, *Earth Planets Space,* **72**(191), doi:10.1186/s40623-020-01333-9.
Bernauer, M., Fichtner, A. & Igel, H., 2009. Inferring earth structure from combined measurements of rotational and translational ground motions, *Geophysics,* **74**(6), WCD41–WCD47.
Bernauer, M., Fichtner, A. & Igel, H., 2012. Measurements of translation, rotation and strain: new approaches to seismic processing and inversion, *J. Seismol.,* **16**(4), 669–681.
Browaeys, J.T. & Chevrot, S., 2004. Decomposition of the elastic tensor and geophysical applications, *J. geophys. Int.,* **159**(2), 667–678.
Cheadle, S.P., Brown, R.J. & Lawton, D.C., 1991. Orthorhombic anisotropy: a physical seismic modeling study, *Geophysics,* **56**(10), 1603–1613.
Cochard, A. *et al.*, 2006. Rotational motions in seismology: theory, observation, simulation, in *Earthquake Source Asymmetry, Structural Media and Rotation Effects,* pp. 391–411, Springer-Verlag.
Corrigan, D., Justice, M.G.J. & Neitzel, E.B., 1986. Estimate of shear-wave anisotropy using multicomponent seismic data, in *SEG Technical Program Expanded Abstracts 1986,* pp. 709–709, Society of Exploration Geophysicists.
Crampin, S., 1977. A review of the effects of anisotropic layering on the propagation of seismic waves, *J. geophys. Int.,* **49**(1), 9–27.
Crampin, S., 1984. Effective anisotropic elastic constants for wave propagation through cracked solids, *J. geophys. Int.,* **76**(1), 135–145.
Dewangan, P. & Grechka, V., 2003. Inversion of multicomponent, multi-azimuth, walkaway VSP data for the stiffness tensor, *Geophysics,* **68**(3), 1022–1031.
Donner, S., Igel, H., Hadziioannou, C. & the Romy, group, 2018. Retrieval of the seismic moment tensor from joint measurements of translational and rotational ground motions: sparse networks and single stations, in *Moment Tensor Solutions,* pp. 263–280, Springer International Publishing.
Edme, P. & Yuan, S., 2016. Local dispersion curve estimation from seismic ambient noise using spatial gradients, *Interpretation,* **4**(3), SJ17–SJ27.
Fichtner, A. & Igel, H., 2009. Sensitivity densities for rotational ground-motion measurements, *Bull. seism. Soc. Am.,* **99**(2B), 1302–1314.
Hadziioannou, C., Gaebler, P., Schreiber, U., Wassermann, J. & Igel, H., 2012. Examining ambient noise using colocated measurements of rotational and translational motion, *J. Seismol.,* **16**(4), 787–796.
Helbig, K. & Thomsen, L., 2005. 75-plus years of anisotropy in exploration and reservoir seismics: a historical review of concepts and methods, *Geophysics,* **70**(6), 9ND–23ND.
Hess, H., 1964. Seismic anisotropy of the uppermost mantle under oceans, *Nature,* **203,** 629–631.
Igel, H., Schreiber, U., Flaws, A., Schuberth, B., Velikoseltsev, A. & Cochard, A., 2005. Rotational motions induced by the m8.1 tokachi-oki earthquake, Sseptember 25, 2003, *Geophys. Res. Lett.,* **32**(8), doi:10.1029/2004gl022336.
Igel, H., Cochard, A., Wassermann, J., Flaws, A., Schreiber, U., Velikoseltsev, A. & Dinh, N.P., 2007. Broad-band observations of earthquake-induced rotational ground motions, *J. geophys. Int.,* **168**(1), 182–196.
Keil, S., Wassermann, J. & Igel, H., 2020. Single-station seismic microzonation using 6c measurements, *J. Seismol*., doi:10.1007/s10950-020-09944-1.
Lindsey, N.J. & Martin, E.R., 2021. Fiber-optic seismology, *Annu. Rev. Earth Planet. Sci.,* **49**(1), null. doi:10.1146/10.1146/annurev-earth-072420-065213.
Love, A., 1892. *The Mathematical Theory of Elasticity*. Cambridge: At the University Press.
Morelli, A., Dziewonski, A.M. & Woodhouse, J.H., 1986. Anisotropy of the inner core inferred fromPKIKPtravel times, *Geophys. Res. Lett.,* **13**(13), 1545–1548.
Musgrave, M. J.P., 1970. *Crystal Acoustics: Introduction to the Study of Elastic Waves and Vibrations in Crystals,* Holden-Day.
Pancha, A., Webb, T.H., Stedman, G.E., McLeod, D.P. & Schreiber, K.U., 2000. Ring laser detection of rotations from teleseismic waves, *Geophys. Res. Lett.,* **27**(21), 3553–3556.
Pham, N.D., Igel, H., de la Puente, J., Käser, M. & Schoenberg, M.A., 2010. Rotational motions in homogeneous anisotropic elastic media, *Geophysics,* **75**(5), D47–D56.
Schoenberg, M. & Helbig, K., 1997. Orthorhombic media: modeling elastic wave behavior in a vertically fractured earth, *Geophysics,* **62**(6), 1954–1974.
Sollberger, D., Greenhalgh, S.A., Schmelzbach, C., Van Renterghem, C. & Robertsson, J.O.A., 2017. 6-c polarization analysis using point measurements of translational and rotational ground-motion: theory and applications, *J. geophys. Int.,* **213**(1), 77–97.
Sollberger, D. *et al.*, 2020. Seismological processing of six degree-of-freedom ground-motion data, *Sensors,* **20**(23), doi:10.3390/s20236904.
Song, X., 1997. Anisotropy of the earth's inner core, *Rev. Geophys.,* **35**(3), 297–313.
Stein, S. & Wysession, M., 2002. *An Introduction to Seismology, Earthquakes, and Earth Structure,* John Wiley and Sons Ltd.
Tang, L. & Fang, X., 2021. Generation of 6-C synthetic seismograms in stratified vertically transversely isotropic media using a generalized reflection and transmission coefficient method, *J. geophys. Int.,* **225**(3), 1554–1585.
Thomsen, L., 1986. Weak elastic anisotropy, *Geophysics,* **51**(10), 1954–1966.
Van Buskirk, W.C., Cowin, S.C. & Carter, R., 1986. A theory of acoustic measurement of the elastic constants of a general anisotropic solid, *J. Mater. Sci.,* **21**(8), 2759–2762.
Wang, Z., 2002. Seismic anisotropy in sedimentary rocks, part 2: laboratory data, *Geophysics,* **67**(5), 1423–1440.
Wassermann, J., Wietek, A., Hadziioannou, C. & Igel, H., 2016. Toward a single-station approach for microzonation: Using vertical rotation rate to estimate love-wave dispersion curves and direction finding, *Bull. seism. Soc. Am.,* **106**(3), 1316–1330.
Woodhouse, J.H., Giardini, D. & Li, X.-D., 1986. Evidence for inner core anisotropy from free oscillations, *Geophys. Res. Lett.,* **13**(13), 1549–1552.
Yuan, S., Simonelli, A., Lin, C.-J., Bernauer, F., Donner, S., Braun, T., Wassermann, J. & Igel, H., 2020. Six degree-of-freedom broadband ground-motion observations with portable sensors: Validation, local earthquakes, and signal processing, *Bull. seism. Soc. Am.,* **110**(3), 953–969.

APPENDIX A: MATERIALS IN THIS STUDY

Properties of the VTI materials *Taylor Sandstone* and *Mesaverde calcareous Sandstone* are summarized in Table A1. The applied orthorhombic material is the industrial laminate *phenolic CE* with the following elastic tensor (Cheadle *et al.* 1991):

$$\mathbf{C} = \begin{pmatrix} 17.443 & 7.462 & 7.008 & 0 & 0 & 0 \\ & 15.445 & 6.097 & 0 & 0 & 0 \\ & & 11.67 & 0 & 0 & 0 \\ & & & 3.135 & 0 & 0 \\ & \mathbf{sym.} & & & 3.518 & 0 \\ & & & & & 3.768 \end{pmatrix} \text{GPa} \qquad \text{(A1)}$$

Table A1. Properties of VTI materials applied in this study. Selected from Thomsen (1986). α_0 and β_0 are vertical *P*- and *S*-wave velocities, respectively. ρ is the density. ϵ, δ and γ are Thomsen parameters where ϵ drives the ratio between horizontal and vertical *P*-wave velocities, γ the ratio between horizontal and vertical *S*-wave velocities and δ influences *P*- and *SV*-wave velocities at intermediate angles.

VTI medium	Taylor Sandstone	Mesaverde calcareous Sandstone
$\alpha_0[\mathrm{m\,s^{-1}}]$	3368	5460
$\beta_0[\mathrm{m\,s^{-1}}]$	1829	3219
ϵ	0.11	0.00
δ	−0.035	−0.264
γ	0.255	−0.007
$\rho[\mathrm{kg\,m^{-3}}]$	2500	2690

APPENDIX B: PROPAGATION DIRECTION DETERMINATION WITH SEVEN COMPONENTS

Considering the plane-wave solutions for acceleration (eq. 2), rotation rate (eq. 3) and strain rate (eq. 4), it is possible to find an expression for the direction of propagation through the formulation of ratios between rotations and strain.

$$\frac{\dot{\Omega}_2}{\dot{\epsilon}_{33}} = \frac{1}{2}\frac{v_3 n_1 - v_1 n_3}{v_3 n_3} = \frac{1}{2}\left(\frac{n_1}{n_3} - \frac{v_1}{v_3}\right)$$
$$\frac{\dot{\Omega}_1}{\dot{\epsilon}_{33}} = \frac{1}{2}\frac{v_2 n_3 - v_3 n_2}{v_3 n_3} = \frac{1}{2}\left(\frac{v_2}{v_3} - \frac{n_2}{n_3}\right) \tag{B1}$$

Eqs (B1) can be solved for v_1 and v_2, respectively. Assuming $v_3 = 1$ and subsequent normalization yields

$$v = \frac{1}{\sqrt{\left(-\frac{2\dot{\Omega}_2}{\dot{\epsilon}_{33}} + \frac{n_1}{n_3}\right)^2 + \left(\frac{2\dot{\Omega}_1}{\dot{\epsilon}_{33}} + \frac{n_2}{n_3}\right)^2 + 1}} \begin{pmatrix} -\frac{2\dot{\Omega}_2}{\dot{\epsilon}_{33}} + \frac{n_1}{n_3} \\ \frac{2\dot{\Omega}_1}{\dot{\epsilon}_{33}} + \frac{n_2}{n_3} \\ 1 \end{pmatrix} \tag{B2}$$

This equation can be applied to isolated wave fronts and hence allows to break the assumption of constant propagation direction between the three arriving body waves. It is more flexible than the 6C method because it does not rely on anisotropic properties of the medium. This formulation was not further analysed in the results section since it did not considerably contribute to the main goal of this study which was to show the feasibility of the elastic tensor inversion with a single 6C/7C sensor. It will be subject to future research.